analytical chemistry

pubs.acs.org/ac Article

Pressure-Based Biosensor Integrated with a Flexible Pressure Sensor and an Electrochromic Device for Visual Detection

Zhenzhong Yu, Guoneng Cai, Xiaolong Liu, and Dianping Tang*

Cite This: *Anal. Chem.* 2021, 93, 2916−2925 Read Online

ACCESS | Metrics & More | Article Recommendations | Supporting Information

ABSTRACT: This work demonstrated a pressure-based biosensor integrated with a flexible pressure sensor and an electrochromic device for visual detection. Initially, a sandwich-type immunoreaction for target carcinoembryonic antigen (CEA, as a model analyte) was carried out using the capture antibody (cAb) and platinum nanoparticles-labeled detection antibody (PtNPs-dAb) in a reaction cell. The added hydrogen peroxide (H_2O_2) could be catalyzed by the PtNPs to generate oxygen (O_2). In a sealed chamber, the pressure increased with the overflowing O_2. Meanwhile, a skin-inspired flexible pressure sensor with excellent sensing performance was fabricated to monitor the pressure change in real time. Thus, the electrical signal of the pressure sensor could reveal the target concentration. Moreover, a voltage-regulated electrochromic device based on polyaniline (PANI) and tungsten oxide (WO_3) was integrated into the platform to provide a visualized readout. According to the electrical signal of the pressure sensor, the electrochromic device would change its color from green to blue, which also revealed the target concentration and could be observed by the naked eye. Under optimal conditions, the biosensor presented a high sensitivity for CEA in a detectable range of 0.2−50 ng/mL. The limit of detection (LOD) was 94 pg/mL. The selectivity, reproducibility, and accuracy were also satisfying. Furthermore, this immunoassay gives a path for developing visualized biosensors in point-of-care settings.

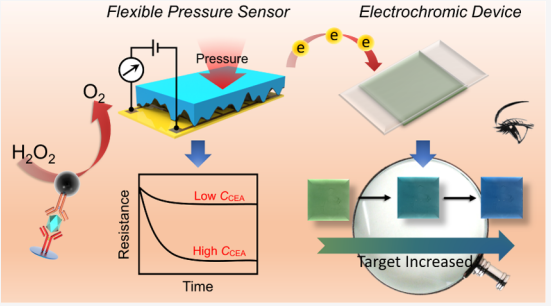

Owing to the explosive development of advanced biomaterials and fabrication technologies, researchers are able to design innovative biosensors with high sensitivity and portable instruments for disease-related biomarkers.[1−3] So far, traditional standard methods adopted in laboratory scenarios are mainly focused on mass spectrometric,[4,5] electrochemical,[6,7] and optical spectrometric methods.[8,9] They allow sensitive, reliable, and accurate measurements, but most of them would suffer from high cost, bulky instruments, and sophisticated operations. These drawbacks restrict their applications in field works and point-of-care testing. Recently, pressure as a classical physical parameter has been used to translate the biomolecule recognition events into measurable signal outputs, relying on the decomposition of H_2O_2 to O_2.[10−13] Because of its user-friendly operations, high sensitivity, low cost, and portable devices, the pressure-based bioassays are considered having great potential in home healthcare and point-of-care settings, which is worthwhile to further research.

Visual detection is a popular trend toward the miniaturization and simplification of the biosensors, which can directly observe the detection results by the naked eye without other equipment.[14,15] Colorimetric method is an effective signal output route, including noble-metal etching,[16,17] small molecular oxidation,[18,19] and electrochromism.[20,21] In these strategies, the visible color change (about 400−700 nm) is usually designed to reflect the biomolecule recognition events and processes. Especially, numerous electrochromic materials such as tungsten trioxide (WO_3), polyaniline (PANI), and Prussian blue (PB) can easily switch their color with the applied potential change, which is originated from the extraction and intercalation of ions during the electrochemical oxidation and reduction.[22] With the desirable advantages of reversible color change, long cycle life, and rapid response in signal transduction, the electrochromic devices are widely applied in smart sensing platforms as the visualized signal readout. Yang et al. established a portable photoelectrochemical device integrating with a WO_3-based electrochromic tablet for visual analysis of pyrophosphate ion.[23] Zhai et al. demonstrated an electrochromic sensing platform for carcinoembryonic antigen based on the steric hindrance effects, and the PB-based bipolar electrode was used as the indicator.[24] Therefore, the electrochromic method provides a path to design portable and visualized signal readouts.

However, a significant issue that remained to be solved is how to combine the electrochromic method with the pressure-

Received: October 25, 2020
Accepted: January 14, 2021
Published: January 25, 2021

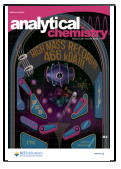

https://dx.doi.org/10.1021/acs.analchem.0c04501
Anal. Chem. 2021, 93, 2916−2925

based bioassay to establish a visualized sensing platform. Fortunately, in our previous works, we successfully constructed a series of pressure-based bioassays using flexible pressure sensors as the signal readout.[25,26] The flexible pressure sensors are able to transduce external pressure into electrical signals (e.g., current, resistance, and capacitance) in real time.[27] By associating with the pressure sensor, the electrochromic device will give color feedback to the pressure according to the electrical signal. In addition, the color change also provides a visualized result readout for the bioassay. Therefore, the sensing performance of the flexible pressure sensor to pressure is a key point in the fabrication process. Normally, fabricating microstructures on the sensing layer is considered as an effective way to improve the sensing properties. To date, various microstructures have been designed, such as micropyramid,[28] microhemisphere,[29] and micropillar.[30] Nevertheless, these traditional microstructures usually require expensive silicon molds and multistep operations. With billions of years of evolution, nature often offers economical and effective strategies with advantageous properties. For example, the human skin with the spinosum structure has a high sensitivity to external stimuli (pressure and temperature).[31] Therefore, diverse bioinspired flexible pressure sensors have been put forward. Yin et al. demonstrated a sensitive tactile sensor by mimicking the bristles in insects.[32] Chun et al. presented a wearable device with octopus suckers-like microstructure for healthcare applications.[33] Hence, it is rational to believe that the bioinspired structure has the ability to improve the signal transduction of the flexible pressure sensor.

Herein, as a proof of concept, we demonstrate a pressure-based sensing platform integrated with a flexible pressure sensor and an electrochromic device for visual detection of carcinoembryonic antigen (CEA, as a model analyte). Scheme 1A shows the circuit diagram, and Scheme 1B,C displays the major modules of the detection system. In brief, for this bioassay, the target is recognized by the capture antibody (cAb) to form the sandwich-type immunocomplex with the PtNP-labeled detection antibody (dAb) in a reaction chamber. Owing to the excellent catalytic ability of PtNPs, the biomolecule recognition event is able to be effectively transduced into the pressure signal by the decomposition of H_2O_2 to O_2. With the increasing pressure, the prepared flexible pressure sensor is stimulated and occurs an obvious elastic deformation, which leads to a decrease in resistance (Scheme 1B). Thus, the corresponding electrical signal can be considered as a detection signal. Meanwhile, in this circuit, the voltage applied to the linked electrochromic device is influenced by the pressure sensor, causing a change in the displayed color (Scheme 1C). According to this principle, the electrochromic device can also be utilized as a visualized result indicator for direct observation with the naked eye. The main purpose of this work is to exploit a simple and visualized signal readout for the pressure-based bioassay in point-of-care and home healthcare settings.

Scheme 1. (A) Circuit Diagram of the Pressure-Based Immunoassay Platform; (B) Schematic Illustration of the PtNP-Triggered Immunoassay with a Flexible Pressure Sensor Readout; and (C) Structure of the Voltage-Regulated Electrochromic Device as a Visualized Readout

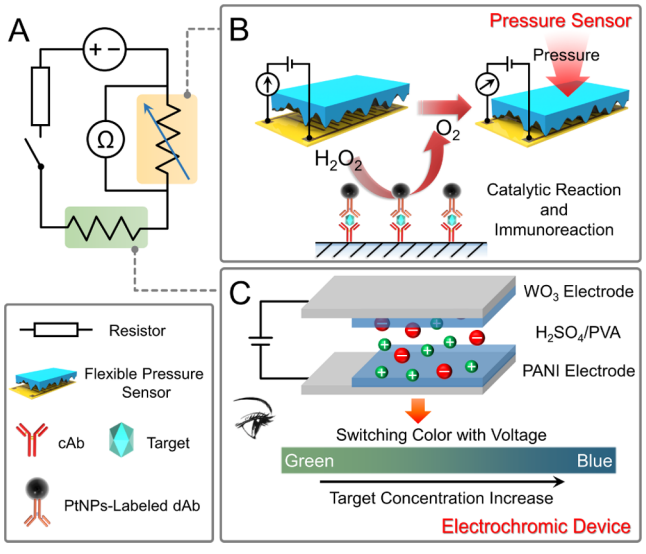

EXPERIMENTAL SECTION

Preparation of the Flexible Pressure Sensor. To obtain the sensing layers with different roughness, commercial abrasive papers with different roughnesses (#120, #240, #320, and #400) and a flat glass sheet were utilized as templates. Poly(dimethylsiloxane) (PDMS, prepared by the base agent and curing agent in a weight ratio of 10:1) was uniformly poured on the cleaned templates and degassed for 30 min. After curing at 70 °C for 3 h, the PDMS films were carefully peeled off. Following that, a layer of conductive polypyrrole (PPy) film was grafted on the PDMS surface. The prepared PDMS film was attached to the glass and vertically immersed into a solution at 4 °C for 4 h, which was mixed by the precooled pyrrole solution (100 μL of pyrrole, 1 mL of HCl, and 15 mL of H_2O) and $FeCl_3$ solution (0.5 g of $FeCl_3$, 1 mL of HCl, and 15 mL of H_2O). After the polymerization reaction, the PPy/PDMS film was washed with water and dried at 60 °C. Finally, the PPy/PDMS film was cut into a piece of 6 × 8 mm^2 and covered on a flexible interdigital electrode. To isolate from the atmosphere, the pressure sensor was further encapsulated by a thin layer of PDMS and polyimide (PI) tape.

Preparation of the Electrochromic Device. The electrochromic device was fabricated by PANI and WO_3 electrodes. Both materials were synthesized by electrodeposition methods using a three-electrode system according to previous papers.[34,35] The fluorine-doped tin oxide (FTO) glass electrode was used as the substrate for electrodeposition. The PANI electrode was prepared in an electrolyte solution (containing 0.5 M Na_2SO_4, 0.5 M H_2SO_4 and 0.05 M aniline) at a constant current of 0.1 mA/cm^2 (vs Ag/AgCl) for 30 min. For the WO_3 electrode, the electrolyte solution contained 12.5 mM Na_2WO_4 and 0.1% H_2O_2 with the pH adjusted to 1.3 by $HClO_4$. The electrodeposition for WO_3 was performed at −0.55 V (vs Ag/AgCl) for 20 min. All electrodes were washed with water. Following that, a gel electrolyte was prepared by totally dissolving 1.5 g of poly(vinyl alcohol) (PVA) in 10 mL of H_2SO_4 solution (1 M) at 90 °C. The cooled H_2SO_4/PVA gel electrolyte was tightly sandwiched between the PANI and WO_3 electrodes by a clamp. Finally, it was dried at 40 °C to remove excess water.

Preparation of the Platinum Nanoparticle-Labeled Detection Antibodies (PtNPs-dAb). First, the H_2PtCl_6 solution (0.26 mL, 2 wt %) was diluted with 9.74 mL of H_2O and heated at 80 °C for 20 min. Then, the ascorbic acid solution (1 mL, 0.4 M) was quickly injected with slight stirring

https://dx.doi.org/10.1021/acs.analchem.0c04501
Anal. Chem. 2021, 93, 2916−2925

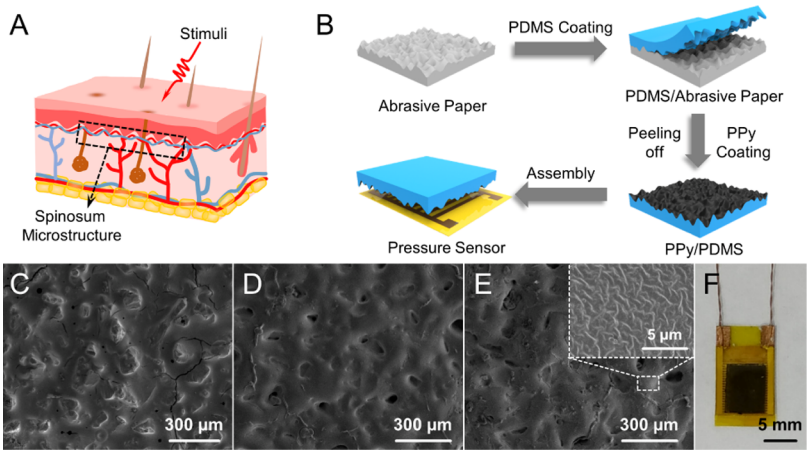

Figure 1. (A) Schematic diagram of the human skin with spinosum structure. (B) Fabrication process of the flexible pressure sensor. SEM images of (C) abrasive paper (#240), (D) the prepared PDMS film, and (E) the PPy/PDMS film. (F) Photograph of the flexible pressure sensor.

and kept at 80 °C for 30 min. Finally, the prepared PtNPs were stored at 4 °C before use. The Pt concentration was 0.18 mg/mL.

The PtNPs-dAb were prepared according to the reported procedure with a minor modification.[36,37] In brief, 25 μL of thiol-poly(ethylene glycol)-acid (SH-PEG-COOH, 2 mg/mL) was added to 5 mL of PtNPs and shaken at room temperature for 2 h. The unconjugated reagents were removed by centrifugation. Then, the PtNPs were redispersed in 5 mL of 2-(*N*-morpholino)ethanesulfonic acid buffer (MES, 0.1 M, pH 5.2) that contained 1-ethyl-3-(3-dimethylaminopropyl) carbodiimide hydrochloride (EDC, 0.4 M) and *N*-hydroxysuccinimide (NHS, 0.1 M) and activated at room temperature for 30 min. After washed repeatedly, the functionalized PtNPs were redispersed in 3 mL of phosphate-buffered saline (PBS, 0.01 M, pH 7.4) to form a homogeneous solution by slight ultrasonic treatment. Following that, 50 μL of dAb (0.5 mg/mL) was added to conjugate with PtNPs and reacted at 4 °C overnight with gentle shaking. The PtNPs-dAb were collected by centrifugation (14 000*g*) at 4 °C for 15 min and washed with PBS three times. Finally, the PtNPs-dAb was dispersed in 3 mL of a storage solution (0.01 M PBS contained 1.0 wt % bull serum albumin and 0.05% Tween 20, pH 7.4) at 4 °C before use.

Immunoassay Procedure. In this immunoassay, the high-binding polystyrene microwell was used as the reaction cell. First, the reaction cell was coated with cAb (50 μL, 10 μg/mL) overnight at 4 °C and washed with washing buffer (0.01 M PBS, 0.05 wt % Tween 20, pH 7.4) three times. Then, it was blocked by 300 μL of blocking buffer (0.01 M PBS, 1.0 wt % bull serum albumin, pH 7.4) at room temperature for 1 h. After washing, the CEA standard or sample (50 μL) was added and incubated at room temperature for 40 min with slight shaking. Thereafter, the washing process was repeated and 100 μL of the dAb-PtNPs was injected to incubate for 40 min. After washing, H_2O_2 (100 μL, 30%) was added and the reaction cell was linked with the pressure sensor and electrochromic device. The reaction cell directly attached to the pressure sensor through a three-dimensional (3D) printing sealed chamber with a cylindrical pipe. The cylindrical pipe could cap the reaction cell tightly. After 8 min, the detection result was simultaneously obtained from the pressure sensor measured by a digital multimeter (DMM) and the color change of the electrochromic device.

RESULTS AND DISCUSSION

Fabrication and Characterization of the Flexible Pressure Sensor. In this work, the pressure sensor was assembled by an elastic sensing layer and a flexible electrode layer. To obtain excellent sensing performance, it was necessary to fabricate the microstructure on the sensing layer. The human skin with special spinosum microstructure was a critical tissue to sense environmental stimuli, such as pressure and temperature (Figure 1A). Inspired by this natural structure, we adopted a facile method to shape a multiridged microstructure with random distribution on the surface of the sensing layer using abrasive paper as the template. The detailed fabrication process of the pressure sensor is presented in Figure 1B. PDMS was first coated on the abrasive paper and cured to obtain a patterned elastic substrate. A scanning electron microscope (SEM) was used to further evaluate the surface morphology. Herein, the abrasive paper with the roughness of #240 was used as an example to explain this fabrication process. As shown in Figure 1C, the surface of the abrasive paper was covered with irregular gravel particles, which were about 80−120 μm in size. Thus, the imprinted PDMS film was endowed with an inverse microstructure to the abrasive paper template, which showed interconnected ridges and randomly dispersive holes (Figure 1D). These irregular ridges played a critical role in the sensitivity and accuracy of the pressure devices in pressure perception because they provided strongly concentrated local stress at the contact areas when the pressure was loaded. Subsequently, the patterned PDMS film was treated in a pyrrole solution to decorate a uniform and conductive PPy film. As shown in Figure 1E, the structure feature of the PPy-coated PDMS film (PPy/PDMS) did not appear significantly different from the original PDMS film. From the cross-sectional view, the PPy film was closely and tightly attached to the PDMS substrate with a thickness of about 6 μm (Figure S1A). However, due to the modification of PPy, the smooth PDMS surface became quite rough, which was full of wrinkles and ripples (inset in Figures 1E and S1B). It was speculated to be caused by the pyrrole polymerization and solution evaporation. Moreover, the Raman spectra in Figure S2 with typical PPy peaks of 1043, 1327, and 1570 cm^{-1} definitely indicated the successful preparation of PPy on PDMS substrate.[38] The prepared PDMS and PPy/PDMS films are displayed in Figure S3. Both of them showed excellent flexibility and bendability. Finally, the PPy/PDMS film as the

https://dx.doi.org/10.1021/acs.analchem.0c04501
Anal. Chem. 2021, 93, 2916−2925

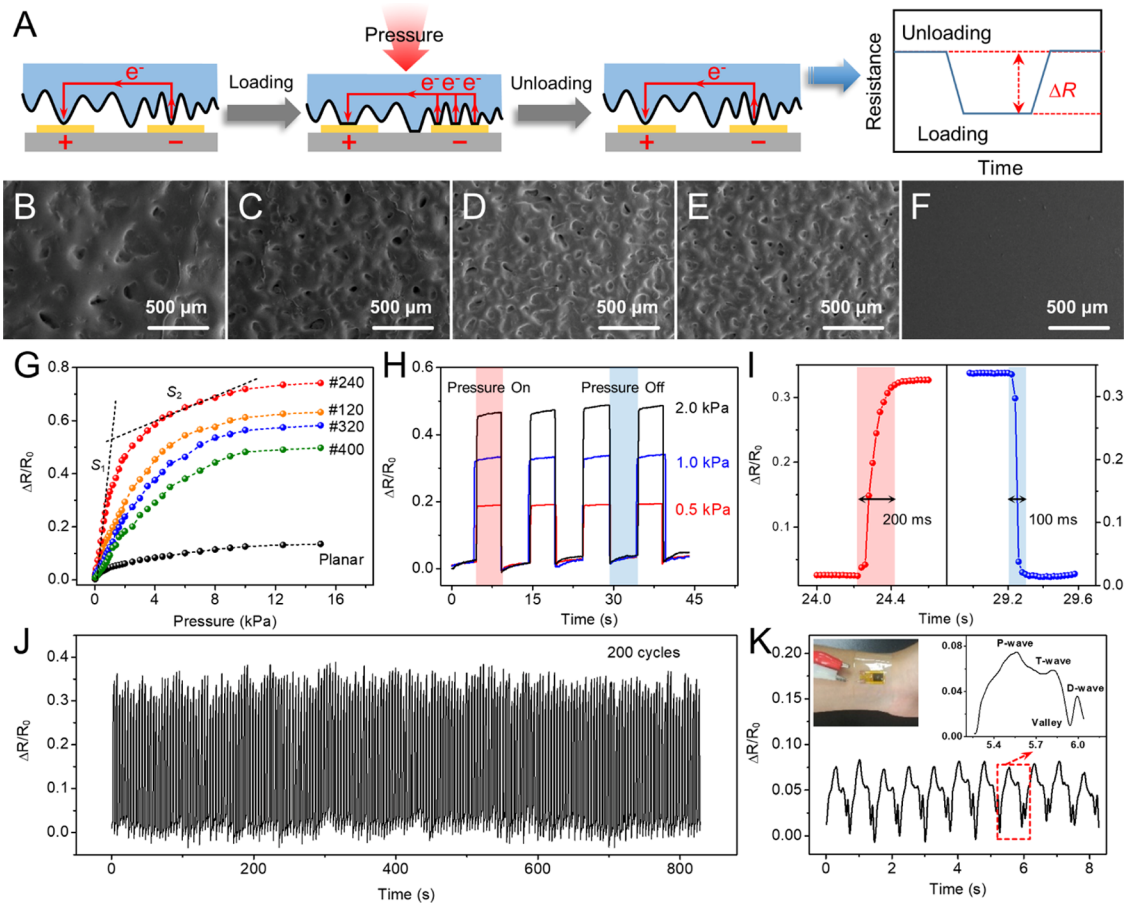

Figure 2. (A) Sensing mechanism of the flexible pressure sensor. SEM images of the PDMS films prepared by different abrasive papers: (B) #120, (C) #240, (D) #320, (E) #400, and (F) planar glass sheet. (G) Pressure responses for pressure sensors prepared by different abrasive papers (#120, #240, #320, #400) and planar glass. (H) Real-time pressure responses of the pressure sensor prepared by #240 abrasive paper at different pressures (0.5, 1.0, and 2.0 kPa). (I) Response time and recovery time of the pressure sensor prepared by #240 abrasive paper. (J) Durability test of the pressure sensor prepared by #240 abrasive paper for 200 loading/unloading cycles at the pressure of 1.0 kPa. (K) Detection of wrist pulse using the pressure sensor prepared by #240 abrasive paper; insets: (left) photograph of the pressure sensor assembled on the wrist and (right) magnified view of the red box.

sensing layer was assembled with a flexible interdigital electrode and encapsulated by a thin layer of PDMS and PI tape to isolate the air. The employed interdigital electrode is shown in Figure S4A. There were 20 pairs of small gold electrodes on PI substrate, and each gold electrode was about 90 μm (Figure S4B). The fabricated pressure sensor is shown in Figure 1F.

For such a pressure sensor, the working mechanism is illustrated in Figure 2A. In the initial state, only a few PPy/PDMS ridges contacted with the gold electrodes to form actual conductive channels, leading to a high initial resistance. When an external pressure was loaded on the sensor, most of the force was concentrated on the ridges near the contact regions, resulting in huge elastic deformation of the sensing layer. Meanwhile, it would temporarily cause numerous conductive paths and a decrease in resistance between the sensing and electrode layers. Moreover, the higher pressure would cause more obvious deformation and resistance to decrease. In contrast, when the pressure was released, the microstructure would recover to its original shape because of the excellent elasticity of PDMS. Therefore, the electrical signal would return to the initial level. In this case, the pressure was sensitively perceived by the pressure sensor.

To measure the sensing performance, different pressure values were loaded on the sensor, which was achieved by loading objects with different masses. Logically, because of the designed structure, it was evident that the surface microstructure was a critical factor for the sensing performance. Therefore, we regulated the roughness of the sensing layer using the abrasive papers with different meshes (#120, #240, #320, and #400) and a planar layer was used as the control sample. Figure 2B–F shows the typical SEM images of these sensing layers, which clearly display different surface microstructures. The relative resistance variation ($\Delta R/R_0 = (R_0 - R)/R_0$, where R_0 and R are the initial resistance and the resistance under pressure of the pressure sensor, respectively) was used to characterize the pressure response. The $\Delta R/R_0$ values of these sensors under different pressures are plotted in Figure 2G. As shown in Figure 2G, the pressure responses of all devices exhibited rising trends, while the sensors with patterned sensing layers were obviously higher than the planar sensor. Notably, the pressure responses of patterned sensors were divided into two regions. The relative resistance variation first increased rapidly with the increasing pressure in the low-pressure region (<1.5 kPa). Then, it gradually slowed down and reached a maximum in the high-pressure region (>1.5 kPa). The typical pressure response behavior of the

https://dx.doi.org/10.1021/acs.analchem.0c04501
Anal. Chem. 2021, 93, 2916−2925

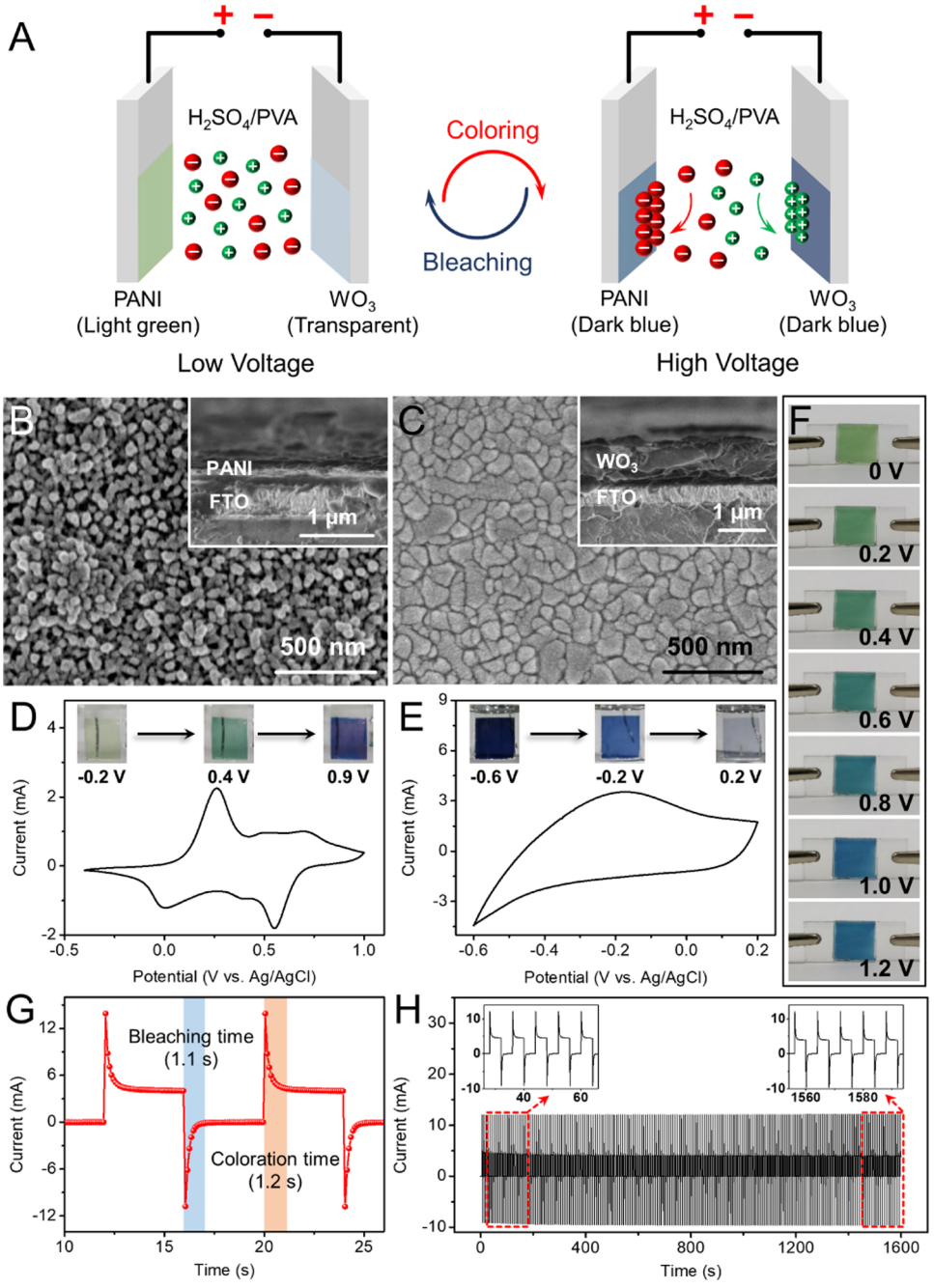

Figure 3. (A) Working mechanism of the electrochromic device. SEM images of (B) PANI and (C) WO_3; insets: the corresponding magnified SEM images. Cyclic voltammetry curves of (D) PANI and (E) WO_3; insets: photographs of PANI and WO_3 electrodes at different potentials. (F) Photographs of the electrochromic device under different voltages. (G) Color switching time of the device characterized by chronoamperometry. (H) Stability test of the device for 200 cycles between 0 and 0.6 V; inset: magnified views of the red boxes.

piezoresistive sensor was originated from the gradual saturation of PDMS deformation, which decided the formation of conductive paths. To quantitatively describe the sensing performance, the sensitivity (S) was defined as $S = \delta(\Delta R/R_0)/\delta P$ ($\Delta R/R_0$ and P denoted the relative resistance variation and the applied pressure). By comparing, the device prepared by #240 abrasive paper presented the highest sensitivities both in the low-pressure and high-pressure regions, which were 0.542 and 0.023 kPa^{-1}, respectively. The detailed sensitivities of other sensors are listed in Table S1. It was speculated that too large surface roughness (prepared by small mesh abrasive paper) hindered the applied force being concentrated on the ridges, leading to a low sensitivity to the pressure. On the other hand, too small surface roughness (prepared by large mesh abrasive paper) could not provide enough microstructures, which also resulted in poor sensing performance. In conclusion, the experiment results clearly showed that the ridge microstructure could effectively improve the sensing performance of the pressure sensor and the #240 abrasive paper was the most suitable template to shape the microstructure for the sensing layer.

Besides, other important parameters of the sensor were also needed to be evaluated, such as repeatability, reliability, response time, and, durability. As shown in Figure 2H, a series

https://dx.doi.org/10.1021/acs.analchem.0c04501
Anal. Chem. 2021, 93, 2916−2925

of pressures (0.5, 1.0, and 2.0 kPa) were repeatedly loading and unloading on the pressure sensor. It was obvious that the sensor presented corresponding responses according to the pressure values without hysteresis. They kept the same values under the same pressures with small fluctuations, which might be caused by the uncovered PPy film. The relative standard deviation (RSD) of the relative resistivity changes were 3.68, 1.67, and 1.27% when the applied pressures were 0.5, 1.0, and 2.0 kPa, respectively. It meant that the sensor had excellent repeatability. As another important parameter, the response time of this sensor was also investigated. As shown in Figure 2I, the response and recovery times were 200 and 100 ms, respectively. With such a low delay, it was sufficient to satisfy the requirements in practical applications. To further evaluate its durability, the cycling test of the sensor was measured by repeatedly loading and unloading pressure of 1.0 kPa for 200 cycles. There was no obvious fluctuation being observed in the output signal during the whole testing process (Figure 2J). The pressure responses in the starting and ending points were at the same level without significant attenuation (Figure S5), confirming the good durability of the prepared sensor. The reproducibility of different pressure sensors prepared by the same #240 abrasive paper was carried out by testing three parallel pressure sensors. At the same pressure of 1.0 kPa, the relative standard deviation of the pressure response of the three pressure sensors was 11.2%, which meant good inter-batch reproducibility of the pressure sensor. Moreover, the pressure sensor could also be applied to biological monitoring. Figure 2K shows the typical pressure response to human wrist pulse. The typical features of the wrist pulse could be clearly identified, including percussion wave (P-wave), tidal wave (T-wave), valley, and diastolic wave (D-wave), which provided lots of useful information for healthcare (inset in Figure 2K). However, in this work, as a proof-of-concept, all operations were carried out at a stationary temperature (25 °C). Obviously, for such a sensor, the ambient temperature and atmospheric pressure would influence its accuracy. Thus, it needed to be corrected when it was used in different conditions. This might be a deficiency of the sensor. Overall, these results sufficiently indicated that the ridge microstructure-based pressure sensor possessed remarkable sensing performance.

Fabrication and Characterization of the Electrochromic Device. The electrochromic device was employed as a visualized result readout in this immunoassay, which was required to be sensitive to the voltage change. PANI and WO_3 were chosen as the positive and negative electrodes, respectively, because of their matching electrochromic behaviors and compatibility in acidic electrolytes. Namely, PANI was colored from light green to dark blue at high potential and bleached at low potential, while WO_3 was colored from transparent state to dark blue at low potential and bleached at high potential. With the assistance of H_2SO_4/PVA gel electrolyte, an electrochromic device with a sandwich structure was formed (Figure S6). The electrochromic mechanism is illustrated in Figure 3A. At low voltage, the SO_4^{2-} and H^+ anions were free in the gel electrolyte. The device was at bleached state with light green PANI and transparent WO_3. With the voltage increasing, the SO_4^{2-} and H^+ anions were intercalated in PANI and WO_3 electrodes, respectively, leading to a colored state. At this state, both PANI and WO_3 became dark blue. Conversely, the ions could also be extracted from the electrodes with the decreasing voltage. Meanwhile, the color recovered to its initial state. The reactions at different electrodes could be demonstrated as follows[34]

Positive electrode

$$\text{PANI (green)} + n{SO_4}^{2-} - 2ne^- \leftrightarrow (\text{PANI}^{2n+})({SO_4}^{2-})_n\text{(blue)}$$

Negative electrode

$$WO_3\text{(transparent)} + 2nH^+ + 2ne^- \leftrightarrow H_{2n}WO_3\text{(blue)}$$

The synergetic color change of the two complementary materials endowed the prepared electrochromic device with outstanding electrochromic performance.

The SEM images of synthesized PANI and WO_3 on FTO substrates are displayed in Figure 3B,C. It could be seen that the PANI was formed by small nanoparticles with a film thickness of 300 nm. For the WO_3, it was stacked with small crystals with a film thickness of 1.2 μm. Furthermore, the Raman spectra of PANI and WO_3 are exhibited in Figure S7. As for PANI, the expected peaks were presented at 1168, 1322, 1486, 1585, and 1624 cm^{-1}, respectively.[39] The spectrum of WO_3 showed the typical peaks at 671 and 956 cm^{-1}, respectively.[40] These characteristic spectra indicated the successful preparations of these electrochromic materials. The electrochemical properties of PANI and WO_3 electrodes were characterized using a three-electrode system in H_2SO_4 solution. The cyclic voltammetry (CV) curves in Figure 3D,E proved the good electrochemical activities and superior electrochromic features. With the potential increasing, the PANI showed three redox peaks with the color changes from light green to green to dark blue. The first and third redox peaks were assigned to the exchanges of lucoemeraldine/emeraldine and emeraldine/pernigraniline states of PANI, respectively, and the second redox peaks were the over-oxidation products.[41] In contrast, the color of WO_3 changed from blue to transparent with the increasing potential because of the extraction of H^+.

The color response to the applied voltage was a significant property for the electrochromic device. As shown in Figure 3F, it was clearly observed that the color changed from green to blue with the increasing voltage from 0 to 1.2 V using a two-electrode system. Moreover, the sequential color change between 0 to 1.0 V was recorded in Video S1. The color switching also was an important property for its applications, which was analyzed by chronoamperometry with continuously stepping the voltage between 0 and 0.6 V. The color switching times could be obtained from the chronoamperometry curve, which were 1.2 s for coloration time and 1.1 s for bleaching time (Figure 3G). To evaluate the cyclic stability, the device was tested by chronoamperometry for 200 cycles between 0 and 0.6 V. The anodic and cathodic peak currents did not appear obvious difference during this process, meaning excellent stability (Figure 3H). These remarkable advantages of the multicolor response, short switching time, and high stability indicated that the prepared electrochromic device had great potential as a visualized readout in this immunoassay.

Feasibility of the Analytical Strategy. Before the proposed immunoassay was implemented, two confusing issues should be clarified. The first one was whether the electrochromic device could rapidly reflect the voltage change of the pressure sensor; the other one was whether the pressure sensor could sensitively monitor the generated gas pressure. To

https://dx.doi.org/10.1021/acs.analchem.0c04501
Anal. Chem. 2021, 93, 2916−2925

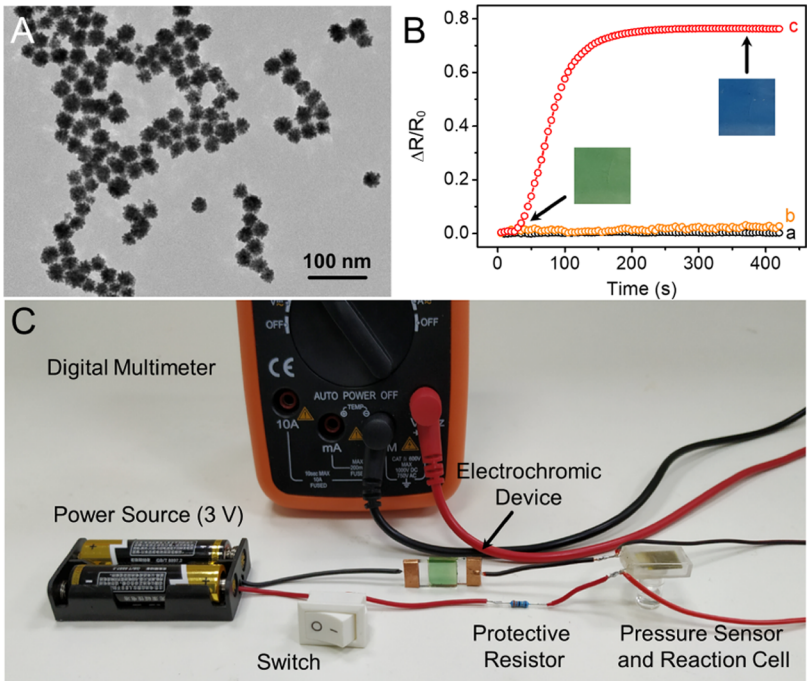

Figure 4. (A) TEM image of PtNPs. (B) Pressure responses of the pressure sensor with different additives: (a) blank group, (b) H_2O_2 (100 μL), and (c) H_2O_2 (100 μL) and PtNPs (2 μL, 0.18 mg/mL); insets: the corresponding photographs of the electrochromic device connected with the pressure sensor at different pressures. (C) Photograph of the assembled pressure-based biosensor with a visualized readout.

solve the first problem, we connected the pressure sensor and the electrochromic device in series. When the pressure was not loaded, the pressure sensor had a large resistance and a high applied voltage. Correspondingly, the electrochromic device obtained a low applied voltage and appeared green. In contrast, when the pressure was loaded, the pressure sensor had a small resistance and a low applied voltage, causing the electrochromic device to keep at a high voltage and appeared blue. This testing process is shown in Video S2. For the other issue, the decomposition of H_2O_2 that was catalyzed by PtNPs was chosen as the gas-generating reaction in this work because of its high gas generation efficiency and nontoxic products. In Figure 4A, the transmission electron microscope (TEM) image of the synthesized PtNPs showed that the PtNPs were well monodispersed with a mean size of 25 nm (Figure S8). And then, we simply mixed H_2O_2 (100 μL) with excess PtNPs (2 μL, 0.18 mg/mL) and used the pressure sensor to measure the gas generation in a sealed device. Figure 4B shows the pressure response curves with different additives. A strong pressure response was only observed when the PtNPs and H_2O_2 existed simultaneously. Conversely, there was almost no pressure response for the blank group; and a weak pressure response appeared when H_2O_2 was added alone, which was originated from the natural decomposition of H_2O_2. Thus, the pressure sensor could achieve the purpose of real-time pressure detection for the gas-generating reaction. In addition, the electrochromic device also presented obviously different colors in the process. Therefore, we speculated that the pressure sensor and electrochromic device could be used as dual result readouts to exploit the immunoassay by adopting the PtNP-labeled strategy.

Analysis Performance. To integrate these components, a sensing platform was assembled (Figure 4C), including a power source (3 V), the prepared pressure sensor in a sealed chamber, a reaction cell, the electrochromic device, a digital multimeter, a protective resistor, and a switch. The reaction cell was attached to the pressure sensor using a 3D printing sealed chamber, which had a cylindrical pipe to cap the reaction cell tightly (Figure S9). The circuit diagram is shown in Scheme 1A. Additionally, to obtain a good sensing performance, some factors that might influence the result were investigated, such as immunoreaction time, PtNPs catalysis time, and H_2O_2 concentration (Figure S10). Under optimal conditions, the sensing ability of this immunoassay was analyzed by detecting a series of CEA standards with different concentrations. The pressure response (i.e., relative resistance variation, $\Delta R/R_0$) measured by DMM was positively correlated with CEA concentration (C_{CEA}) in Figure 5A (inset). As shown in Figure 5A, $\Delta R/R_0$ and the logarithm of

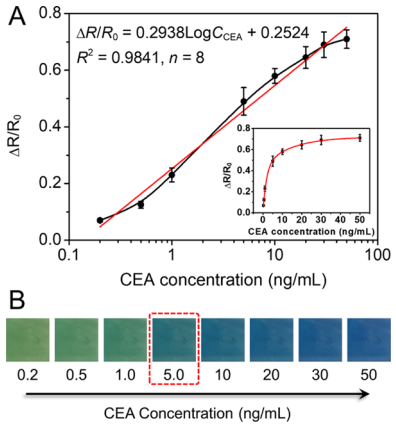

Figure 5. (A) Linear relationship between the pressure response of the pressure sensor and the logarithm of CEA concentration (inset: relationship between $\Delta R/R_0$ and CEA concentration). (B) Photographs of the electrochromic device with different CEA concentrations.

https://dx.doi.org/10.1021/acs.analchem.0c04501
Anal. Chem. 2021, 93, 2916−2925

C_{CEA} presented a good linear relationship ranging from 0.2 to 50 ng/mL, which was calculated as $\Delta R/R_0 = 0.2938 \log C_{CEA} + 0.2524$ ($R^2 = 0.9841$, $n = 8$). Its limit of detection (LOD) estimated by the $3\sigma/K$ rule (the σ and K were the standard deviations of 11 determinations blank groups and the slope of the calibration plot, respectively) was 94 pg/mL. The maximum relative standard deviation (RSD) of all data points was 9.89%, indicating the good reproducibility and precision of our sensor. The generated pressure could be obtained from Figure 2G according to the relative resistance variation. In this assay, the generated pressure ranged from 0.188 to 9.445 kPa with different CEA concentrations (Figure S11). Moreover, as the visualized result output, the electrochromic device presented different colors from green to blue with the increasing C_{CEA} (Figure 5B). Importantly, the normal value of CEA in health human serum was lower than 5 ng/mL,[42] which could be clearly identified from the color change. Thus, the higher or lower CEA levels could be observed by the naked eye, achieving the purpose of portable and visual detection for CEA.

To further clarify the advantages of the proposed immunoassay, some reported methods for the detection of CEA are summarized in Table S2. With the expensive instruments and long detection time, the other biosensors obtained a quite low limit of detections. Although the sensitivity of our method was lower than others, the shorter detention time and simpler readout were achieved in our method. The aim of this work was to establish a portable immunoassay for point-of-care testing. Our strategy adopted the simple pressure readout and electrochromic device as the signal readouts for the quantified and semiquantified detecting, respectively. The pressure sensor with the electrical readout could provide an accurate and sensitive result. Meanwhile, the electrochromic device could be used not only in combination with the pressure sensor but also alone without the electrical readout. When the electrical readout was lacking, the detection results could be provided by the electrochromic device and read by the naked eye directly without other equipment, which was beneficial for its applications in fieldwork and instrument-limited environments. Compared with the light-emitting diode (LED) as an indicator, the electrochromic device could give more information according to a series of colors rather than a "yes/no" answer. And people were more sensitive to color change than light intensity. On the other hand, the threshold value of CEA in human serum (5 ng/mL) was included in the working range, which made the immunoassay meet the requirement of practical application.

The specificity as a significant parameter of the sensor was also evaluated. Some interfering biomolecules that might coexist in human serum were used to investigate the specificity, including prostate-specific antigen (PSA), cancer antigen 125 (CA-125), and α fetoprotein (AFP). As shown in Figure S12, for these interfering biomolecules, the sensor presented weak signal responses, which were close to the blank group. Meanwhile, strong signal responses were achieved in the presence of the CEA target, regardless of alone or mixed with others. Besides, about 87.3% of the initial signal response intensity was obtained after 8 weeks. The response attenuation was presumably caused by the gradual inactivation of the detection antibodies on PtNPs.

To further evaluate the accuracy of the proposed immunoassay, seven human serum specimens were collected from the local hospital (Mengchao Hepatobiliary Hospital, Fujian). These samples were detected by the proposed immunoassay and commercial CEA ELISA kit, respectively. The *t*-test was used for statistical analysis of the results obtained from the two methods (Table 1). The maximal t_{exp} (*t*-experimental) value was lower than the t_{crit} (*t*-critical) value ($t_{crit[0.05,4]} = 2.78$). Moreover, a good linear relationship ($R^2 = 0.9931$) between the two methods with a slope close to "1" was observed in Figure S13. The high agreement of the two methods revealed that the proposed immunoassay had acceptable accuracy and could be preliminarily applied in biological samples.

Table 1. Comparison of the Results Obtained from the Pressure-Based Bioassay and the Commercial ELISA Kit for Human Serum Samples

	method; concentration (mean ± SD, n = 3, ng/mL)[a]		
sample no.	pressure-based bioassay	commercial ELISA kit	t_{exp}[b]
1	26.44 ± 2.56	29.17 ± 2.35	1.36
2	11.28 ± 0.95	12.43 ± 0.94	1.49
3	21.75 ± 1.84	20.66 ± 1.56	0.79
4	1.21 ± 0.11	1.05 ± 0.04	2.34
5	8.73 ± 0.47	7.98 ± 0.56	1.77
6	18.28 ± 1.47	17.64 ± 1.23	0.58
7	35.57 ± 3.13	37.13 ± 2.83	0.64

[a]All samples were measured three times, and the samples with high concentration were appropriately diluted. [b]The calculation process of *t*-test statistical analysis is described in the Supporting Information.

CONCLUSIONS

In summary, as a proof of concept, a portable pressure-based immunoassay is successfully established by integrating with a flexible pressure sensor and an electrochromic device for visual detection. In this sensing platform, the pressure triggered by the reaction of PtNPs and H_2O_2 is employed as a signal converter between the biomolecular recognition event and the measurable signal. This signal transduction principle offers excellent signal amplification due to the outstanding catalytic ability of PtNPs and huge volume change from liquid (H_2O_2) to gas (O_2). The human skin-inspired flexible pressure sensor with a portable electrical readout (i.e., DMM) sensitively measures the pressure signal as the quantified detection result. Moreover, as a visual readout, the electrochromic device also provides a semiquantified detection result with the color change according to the electrical signal of the pressure sensor. Importantly, the electrochromic device provides a portable path for signal readout using the naked eye directly when the electrical readout is lacking. It makes the sensing platform perform with a simple device and suitable for instrument-limited environments. With these intrinsic features of high sensitivity, simple operations, and portable instruments, this detection strategy has great potential to develop innovative biomedical assays for home healthcare and point-of-care settings.

ASSOCIATED CONTENT

Supporting Information

The Supporting Information is available free of charge at https://pubs.acs.org/doi/10.1021/acs.analchem.0c04501.

Materials and reagents; apparatus; SEM images, Raman spectra, and photographs of PPy/PDMS and PDMS films; photograph and optical micrograph of the

https://dx.doi.org/10.1021/acs.analchem.0c04501
Anal. Chem. 2021, 93, 2916−2925

interdigital electrode; sensitivities of the pressure sensors with different surfaces; pressure response before and after cycling test; photographs of the electrochromic device; Raman spectra of PANI and WO_3; size distribution of PtNPs; photographs of the pressure sensor; optimization of experimental conditions; relationship between $\Delta R/R_0$ and CEA concentration; specificity of the pressure-based biosensor; comparison of assayed results with ELISA kit and other methods; and calculation method of *t*-test (PDF)

Sequential color change of the electrochromic device between 0 and 1.0 V (Video S1) (MP4)

Color response of the electrochromic device to the pressure (Video S2) (MP4)

AUTHOR INFORMATION

Corresponding Author

Dianping Tang − *Key Laboratory of Analytical Science for Food Safety and Biology (MOE & Fujian Province), Department of Chemistry, Fuzhou University, Fuzhou 350108, People's Republic of China;* orcid.org/0000-0002-0134-3983; Email: dianping.tang@fzu.edu.cn

Authors

Zhenzhong Yu − *Key Laboratory of Analytical Science for Food Safety and Biology (MOE & Fujian Province), Department of Chemistry, Fuzhou University, Fuzhou 350108, People's Republic of China;* orcid.org/0000-0001-9144-7059

Guoneng Cai − *Key Laboratory of Analytical Science for Food Safety and Biology (MOE & Fujian Province), Department of Chemistry, Fuzhou University, Fuzhou 350108, People's Republic of China*

Xiaolong Liu − *The United Innovation of Mengchao Hepatobiliary Technology Key Laboratory of Fujian Province, Mengchao Hepatobiliary Hospital of Fujian Medical University, Fuzhou 350025, People's Republic of China;* orcid.org/0000-0002-3096-4981

Complete contact information is available at: https://pubs.acs.org/10.1021/acs.analchem.0c04501

Notes

The authors declare no competing financial interest.

ACKNOWLEDGMENTS

The authors acknowledge financial support from the National Natural Science Foundation of China (grant nos. 21874022 and 21675029).

REFERENCES

(1) Farka, Z.; Jurik, T.; Kovar, D.; Trnkova, L.; Skladal, P. *Chem. Rev.* **2017**, *117*, 9973−10042.

(2) Shrivastava, S.; Trung, T.; Lee, N. *Chem. Soc. Rev.* **2020**, *49*, 1812−1866.

(3) Yang, G.; Xiao, Z.; Tang, C.; Deng, Y.; Huang, H.; He, Z. *Biosens. Bioelectron.* **2019**, *141*, No. 111416.

(4) Cao, W.; Jiang, B.; Huang, J.; Zhang, L.; Liu, M.; Yao, J.; Wu, M.; Zhang, L.; Kong, S.; Wang, Y.; Yang, P. *Anal. Chem.* **2019**, *91*, 12435−12443.

(5) Keshishian, H.; Burgess, M.; Specht, H.; Wallace, L.; Clauser, K.; Gillette, M.; Carr, S. *Nat. Protoc.* **2017**, *12*, 1683−1701.

(6) Uliana, C.; Peverari, C.; Afonso, A.; Cominetti, M.; Faria, R. *Biosens. Bioelectron.* **2018**, *99*, 156−162.

(7) Chang, J.; Wang, X.; Wang, J.; Li, H.; Li, F. *Anal. Chem.* **2019**, *91*, 3604−3610.

(8) Cui, Y.; Feng, X.; Wang, Y.; Pan, H.; Pan, H.; Kong, D. *Chem. Sci.* **2019**, *10*, 2290−2297.

(9) Wang, J.; Xia, C.; Yang, L.; Li, Y.; Li, C.; Huang, C. *Anal. Chem.* **2020**, *92*, 4046−4052.

(10) Zhu, Z.; Guan, Z.; Liu, D.; Jia, S.; Li, J.; Lei, Z.; Lin, S.; Ji, T.; Tian, Z.; Yang, C. *Angew. Chem., Int. Ed.* **2015**, *54*, 10448−10453.

(11) Song, Y.; Zhang, Y.; Bernard, P.; Reuben, J.; Ueno, N.; Arlinghaus, R.; Zu, Y.; Qin, L.; Arlinghaus, R.; Zu, Y.; Qin, L. *Nat. Commun.* **2012**, *3*, No. 1283.

(12) Song, Y.; Wang, Y.; Qin, L. *J. Am. Chem. Soc.* **2013**, *135*, 16785−16788.

(13) Zeng, R.; Tao, J.; Tang, D.; Knopp, D.; Shu, J.; Cao, X. *Nano Energy* **2020**, *71*, No. 104580.

(14) Mahmoudi, T.; de la Guardia, M.; Shirdel, B.; Mokhtarzadeh, A.; Baradaran, B. *TrAC, Trends Anal. Chem.* **2019**, *116*, 13−30.

(15) Paterson, S.; de la Rica, R. *Analyst* **2015**, *140*, 3308−3317.

(16) Gu, Y.; Song, J.; Li, M.; Zhang, T.; Zhao, W.; Xu, J.; Liu, M.; Chen, H. *Anal. Chem.* **2017**, *89*, 10585−10591.

(17) Gao, Z.; Deng, K.; Wang, X.; Miro, M.; Tang, D. *ACS Appl. Mater. Interfaces* **2014**, *6*, 18243−18250.

(18) Teng, Y.; Shi, J.; Pong, P. *ACS Appl. Nano Mater.* **2019**, *2*, 7421−7431.

(19) Shi, J.; Zhang, S.; Deng, Q.; Li, Y.; Geng, Z.; Zheng, L.; Tang, B. *Chem. Eng. J.* **2020**, *402*, No. 125737.

(20) Sun, X.; Zhang, H.; Hao, S.; Zhai, J.; Dong, S. *ACS Sens.* **2019**, *4*, 2631−2637.

(21) Pellitero, M.; Guimera, A.; Kitsara, M.; Villa, R.; Rubio, C.; Lakard, B.; Doche, M.; Hihn, J.; Javier Del Campo, F. *Chem. Sci.* **2017**, *8*, 1995−2002.

(22) Thakur, V.; Ding, G.; Ma, J.; Lee, P.; Lu, X. *Adv. Mater.* **2012**, *24*, 4071−4096.

(23) Yang, Q.; Hao, Q.; Lei, J.; Ju, H. *Anal. Chem.* **2018**, *90*, 3703−3707.

(24) Zhai, Q.; Zhang, X.; Xia, Y.; Li, J.; Wang, E. *Analyst* **2016**, *141*, 4518.

(25) Yu, Z.; Cai, G.; Liu, X.; Tang, D. *ACS Appl. Mater. Interfaces* **2020**, *12*, 40133−40140.

(26) Yu, Z.; Cai, G.; Tong, P.; Tang, D. *ACS Sens.* **2019**, *4*, 2272−2276.

(27) Huang, Y.; Fan, X.; Chen, S.; Zhao, N. *Adv. Funct. Mater.* **2019**, *29*, No. 1808509.

(28) Cao, Y.; Li, T.; Gu, Y.; Luo, H.; Wang, S.; Zhang, T. *Small* **2018**, *14*, No. 1703902.

(29) Zhang, Y.; Hu, Y.; Zhu, P.; Han, F.; Zhu, Y.; Sun, R.; Wong, C. *ACS Appl. Mater. Interfaces* **2017**, *9*, 35968−35976.

(30) Park, H.; Jeong, Y.; Yun, J.; Hong, S.; Jin, S.; Lee, S.; Zi, G.; Ha, J. *ACS Nano* **2015**, *9*, 9974−9985.

(31) Lee, Y.; Park, J.; Choe, A.; Cho, S.; Kim, J.; Ko, H. *Adv. Funct. Mater.* **2020**, *30*, No. 1904523.

(32) Yin, B.; Liu, X.; Gao, H.; Fu, T.; Yao, J. *Nat. Commun.* **2018**, *9*, No. 5161.

(33) Chun, S.; Kim, D.; Baik, S.; Lee, H.; Lee, J.; Bhang, S.; Pang, C. *Adv. Funct. Mater.* **2018**, *28*, No. 1805224.

(34) Zhong, Y.; Chai, Z.; Liang, Z.; Sun, P.; Xie, W.; Zhao, C.; Mai, W. *ACS Appl. Mater. Interfaces* **2017**, *9*, 34085−34092.

(35) Zhang, J.; Tu, J.; Cai, G.; Du, G.; Wang, X.; Liu, P. *Electrochim. Acta* **2013**, *99*, 1−8.

(36) Xia, X.; Zhang, J.; Lu, N.; Kim, M. J.; Ghale, K.; Xu, Y.; McKenzie, E.; Liu, J.; Ye, H. *ACS Nano* **2015**, *9*, 9994−10004.

(37) Lin, Y.; Zhou, Q.; Tang, D.; Niessner, R.; Knopp, D. *Anal. Chem.* **2017**, *89*, 5637−5645.

(38) Trchová, M.; Stejskal, J. *J. Phys. Chem. A* **2018**, *122*, 9298−9306.

(39) Trchová, M.; Moravkova, Z.; Blaha, M.; Stejskal, J. *Electrochim. Acta* **2014**, *122*, 28−38.

(40) Santato, C.; Odziemkowski, M.; Ulmann, M.; Augustynski, J. *J. Am. Chem. Soc.* **2001**, *123*, 10639−10649.

(41) Zhang, J.; Tu, J.; Zhang, D.; Qiao, Y.; Xia, X.; Wang, X.; Gu, C. *J. Mater. Chem.* **2011**, *21*, 17316−17324.
(42) Arya, S.; Bhansali, S. *Chem. Rev.* **2011**, *111*, 6783−6809.

https://dx.doi.org/10.1021/acs.analchem.0c04501
Anal. Chem. 2021, 93, 2916−2925